Available online at www.sciencedirect.com
ScienceDirect
Trans. Nonferrous Met. Soc. China 29(2019) 2566−2576
Transactions of Nonferrous Metals Society of China
www.tnmsc.cn

Tuning optical properties of ITO films grown by rf sputtering: Effects of oblique angle deposition and thermal annealing

L. G. DAZA[1], M. ACOSTA[2], R. CASTRO-RODRÍGUEZ[1], A. IRIBARREN[3]

1. Department of Applied Physics, CINVESTAV-IPN, Unity Mérida. 97310 Mérida, Yucatán, México;
2. Materials Science Laboratory, Faculty of Engineering, University of Yucatan, CP 97130 Mérida, Yuc., México;
3. Instituto de Ciencia y Tecnología de Materiales, Universidad de La Habana, Zapata s/n esq. G, Vedado, Plaza, La Habana 10400, Cuba

Received 14 March 2019; accepted 17 October 2019

Abstract: Indium tin oxide (ITO) thin films were prepared using the technique of rf-sputtering with oblique angle deposition (OAD). The films were as-deposited and thermally treated at 250 °C. The combination of substrate inclination and annealing was used for modifying morphological and structural properties that lead to changes of the optical properties. The resulting films show morphology of tilted nanocolumn, fissures among columns, and structural changes. The as-deposited films are structurally disordered with an amorphous component and the annealed films are crystallized and more ordered and the film diffractograms correspond to the cubic structure of In_2O_3. The refractive index could be modified up to 0.3 in as-deposited films and up to 0.15 in annealed films as functions of the inclination angle of the nanocolumns. Similarly, the band gap energy increases up to about 0.4 eV due to the reduction of the microstrain distribution. It is found that the microstrain distribution, which is related to lattice distortions, defects and the presence of fissures in the films, is the main feature that can be engineered through morphological modifications for achieving the adjustment of the optical properties.

Key words: oblique angle deposition; ITO thin films; nanocolumnar morphology; microstrain distribution; optical properties

1 Introduction

Indium tin oxide (ITO) is a transparent conducting oxide (TCO). It is one of the more used TCO in multiple applications in optoelectronic and photovoltaic devices, due to its characteristics as wide band gap (about 3.50−3.75 eV) [1] and high transmittance in the range of visible light, low electrical resistivity and high conductivity [2]. ITO has been widely researched [3] for multiple applications and uses, such as windows layers in solar cells [4], UV-LED [2], touch screen [5], sensors and actuators [6], nanoelectronics [7] and others. A material with adjustable refractive index can improve the performance in photonic and optoelectronic applications, due to the possibility of a suitable optical adaptation [8], where either high or low refractive index can be useful and necessary [9,10]. The adjustment of the optical properties of ITO continues in the focus of investigation due to its multiple prospective applications [11−14].

There are several techniques for the growth of ITO as thin film. For example, sol−gel [15,16], spin coating [17,18], thermal evaporation or physical vapor deposition [19], electron beam irradiation [2], and magnetron sputtering [20−23], among others [24] have been used for obtaining ITO films. Magnetron sputtering technique is one of the most used because of the controllable deposition rate, the good stoichiometric reproducibility and low growth temperatures [25,26].

Oblique angle deposition (OAD) is a useful technique in which, by varying the angular position of the substrate respect to incident vapor flux, it is possible to obtain three-dimensionally nanostructured thin films [27] due to the growth of directionally tilted columns as a consequence of shading effect [28]. The formation and modification of such nanostructured films allow to adjust the optical properties in order to find better performance of optoelectronic devices [8,28]. The crystallinity, i.e., the conditions of crystalline, polycrystalline and amorphous phase of a material, influences the electrical, optical and other properties. Annealing can be used as a recrystallization method [29]

Corresponding author: A. IRIBARREN; E-mail: augusto@imre.uh.cu, a_iribarren@yahoo.com
DOI: 10.1016/S1003-6326(19)65164-2

to modify physical characteristics in the films.

ITO films in solar cells and other optoelectronic devices are usually found between two materials and play the role of light transmission as an optical window, in addition to as conductive material. Convenient optical coupling with those neighboring materials is relevant. For example, in solar cells, a minimal reflection of light is necessary at the interfaces with the ITO film, which can be achieved by adjusting the refractive index.

In this work, ITO thin films were prepared using the technique of rf-sputtering with oblique angle deposition (OAD) combined with annealing of the films. ITO films, as-deposited and thermally annealed at 250 °C, are studied and compared. The effects of combining the angle of incidence of flux and the annealing on the optical properties of the films are reported and discussed.

2 Experimental

ITO thin films were deposited on Corning 2947 glass through the technique of sputtering with an ITO target (90% In_2O_3 and 10% SnO_2) of 91.44 cm in diameter (99.99% in purity from Cathay Advance Materials Limited, China). The substrates were cleaned using an ultrasonic bath in distilled water, acetone and isopropyl alcohol. The distance from target to substrate was 60 mm and the base pressure was 6.66×10^{-3} Pa. The deposition was performed under a rf-power of 80 W at room temperature for 30 min with an Ar pressure of 1.33 Pa. The inclination angles of the substrates respect to the deposition flux were α=0°, 40°, 60° and 80° respect to the normal substrate position (α=0°). The films were cleaved and one of the pieces of each film was annealed at 250 °C in air for 1 h. This annealing temperature was chosen because that temperature is around that for promoting crystallization to avoid possible negative optical effects in the red and infrared region due to growth with substrates at high temperature [30]. Surface and cross-sectional images of the ITO films were obtained by means of a JEOL 7600F field emission scanning electron microscope (FESEM). Structural analysis was accomplished using X-ray diffraction (XRD) in the grazing incidence geometry with an inclination of 1° with a D5000 Siemens X-ray Diffractometer and Cu K_α radiation (λ=1.5406 Å). The diffractograms were registered in the step scan mode with a beam incidence angle of 1° and recorded in 0.02° steps with a step time of 10 s in a 2θ range of 15°−70°. The electrical characterization was carried out with an Ecopia HMS−5000 van der Pauw Measurement System at 300 K. The transmittance spectra were recorded with the help of an Agilent 8453 UV-Vis spectrophotometer with a 0.1 nm resolution, in the range of 300−1050 nm and the optical band gaps were calculated only with direct transitions.

3 Results and discussion

3.1 Morphological analysis

The cross-section and surface SEM images are shown in Fig. 1 for as-deposited and annealed ITO films with substrate inclination α of 0°, 40°, 60° and 80°. The SEM image of the annealed sample with α=80° was deposited during a longer time in order to observe it better, although the measurements were carried out in samples grown during 30 min. The as-deposited films with α=0° look dense with grain size of about 40 nm and smaller as observed from the surface SEM images. In the cross-sectional SEM images, the columnar structures are not seen detailed neither well defined, although it is possible to perceive clearly the morphology of tilted nanocolumns.

However, in annealed films, different grain sizes can be observed from the surface SEM images. In general, the surfaces look like cauliflowers, i.e., conglomerates formed by smaller grains as previously reported [31]. In these cases, the conglomerates range from spheroidal grains of about 50 nm in diameter to big ellipsoidal grains with diameters of about 83 nm, and the average size is around 65 nm. The small grains that compose the conglomerates have diameter of up to 10−20 nm. Besides, fissures with small gaps of up to about 15 nm are present and divide some of these conglomerates in all the as-deposited and annealed films with substrate inclination angles of $\alpha\geq60°$.

The dependence of the nanocolumn tilt angle β as a function of the substrate inclination α is found similar for both as-deposited and annealed samples, as shown in Fig. 2. The behavior of nanocolumn tilt is described by

$$\beta_{\text{fit}} = 34.00°\left[1-\exp\left(\frac{\alpha-3.426}{44.559}\right)\right] \quad (1)$$

where β_{fit} (°) is the fitted value of β (°). The film thickness is presented in Fig. 3. The thickness t (nm) is also similar in as-deposited and annealed films and the behavior respect to the nanocolumn tilt angles is given by

$$t_{\text{fit}} = 895-1.15\exp\left(\frac{\beta_{\text{fit}}-53.2°}{13.6°}\right) \quad (2)$$

Table 1 tabulates the substrate inclination angle α, the fitted nanocolumn tilt angle β_{fit}, the fitted average film thickness t_{fit}, and the average growth rate $\gamma_{\text{fit}}=t_{\text{fit}}/30$. Since the nanocolumn tilt in the films is the physical characteristic that rules the changes of other physical parameters, the fitted nanocolumn tilt angle β_{fit} will be used as variable of reference.

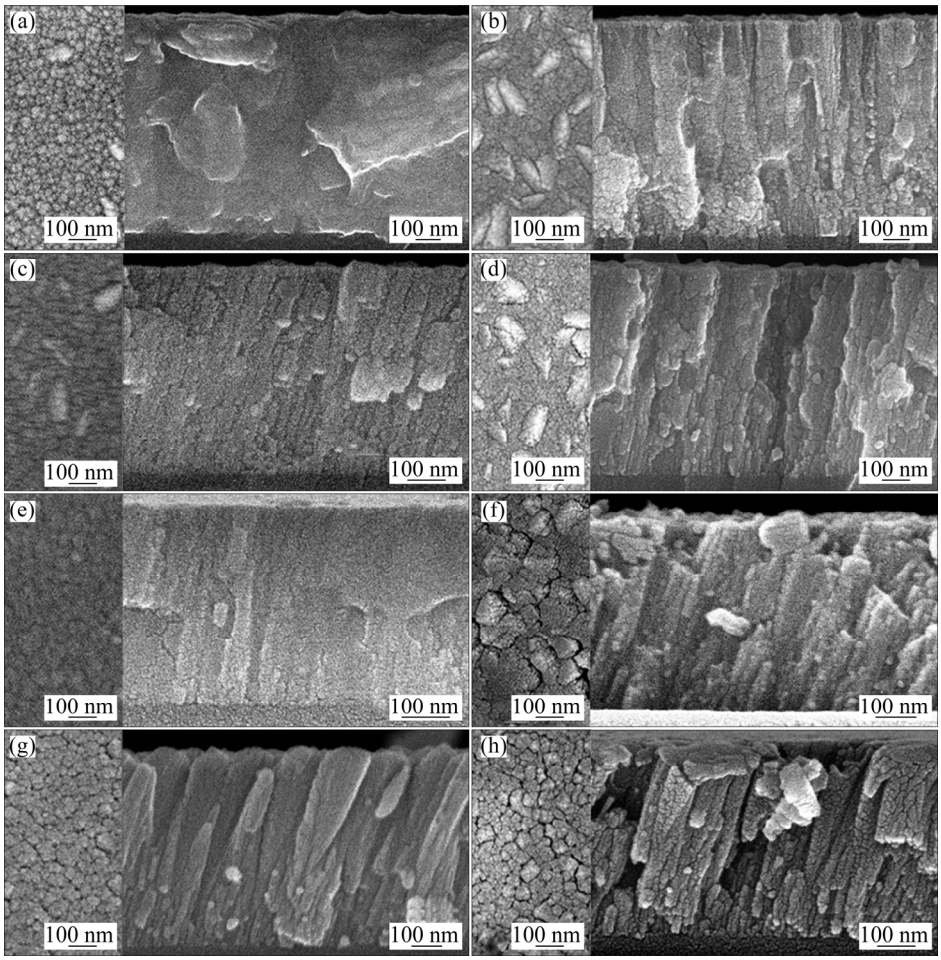

Fig. 1 Surface and cross-sectional FESEM images of as-deposited (a, c, e, g) and annealed (b, d, f, h) ITO thin films: (a, b) α=0°; (c, d) α=40°; (e, f) α=60°; (g, h) α=80°

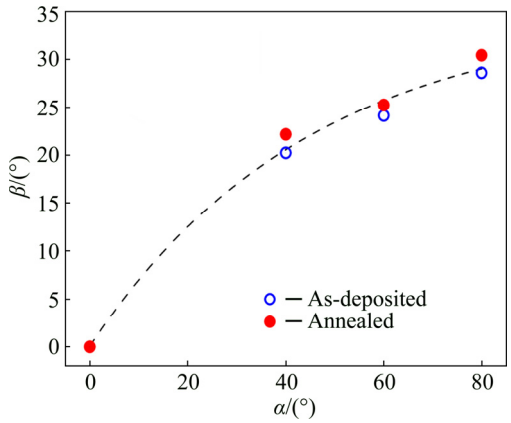

Fig. 2 Nanocolumn tilt angle of as-deposited and annealed ITO films as function of substrate inclination angle

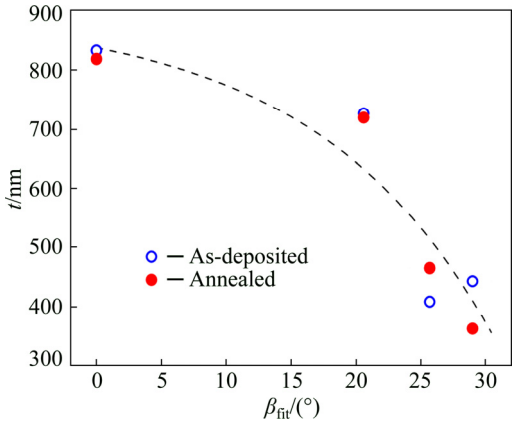

Fig. 3 Film thickness as function of nanocolumn tilt angle in as-deposited and annealed ITO films

3.2 Structural analysis

Figure 4 shows the normalized XRD diffractograms for the as-deposited and annealed ITO thin films grown at substrate inclinations α=0°, 40°, 60 and 80°. The diffractograms of the as-deposited film present not well defined peaks with a halo centered at about $2\theta\approx32°$, which indicates the presence of very disordered or amorphous material, as previously reported [32],

Table 1 ITO thin-film growth parameters

α/(°)	β_{fit}/(°)	t_{fit}/nm	γ_{fit}/(nm·min^{-1})
0	0	838	27.8
40	20.6	633	21.1
60	25.7	510	17.0
80	29.0	406	13.5

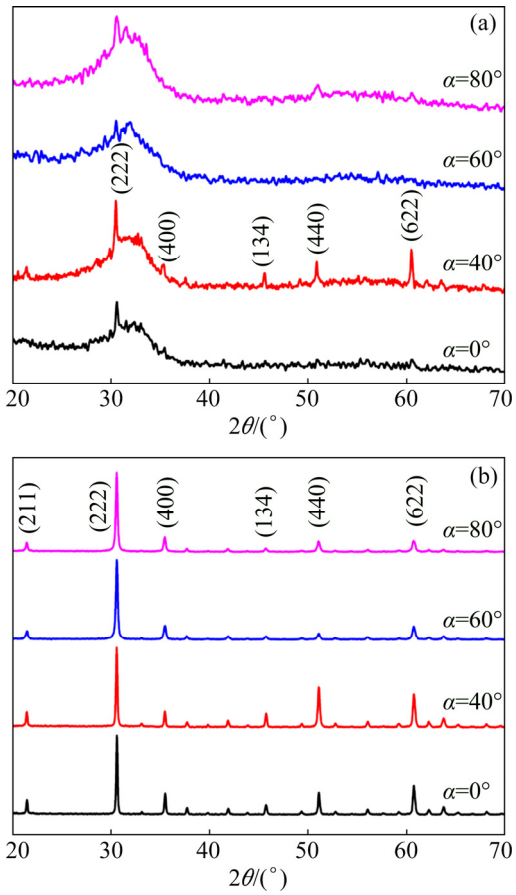

Fig. 4 Normalized diffractograms of as-deposited (a) and annealed (b) ITO thin film with substrate inclinations α=0°, 40°, 60° and 80°

although the peaks can be related to those of In_2O_3 structure [33]. For the films annealed at 250 °C, the diffraction peaks are well defined, which indicates that crystallization and better structural organization take place. Therefore, we only focused on as-deposited and 250 °C-annealed films. The body-centered cubic phase of In_2O_3 can be observed in the 250 °C-annealed films. In the films, the (222) peak is the most intense, but other less-intense peaks are also observed. This feature is also similar to the In_2O_3 pattern, although the peaks are shifted toward higher angles due to the addition of Sn and the formation of a solid solution of Sn in In_2O_3. The 2θ values present random behavior without some tendency under changes of the substrate inclination. Using the most intense peak (222), we calculated that it has an average value $2\theta_{(222)}$=(30.61±0.01)°, which shows that it is shifted respect to the same peak of the pattern $2\theta_0$=30.586°.

In order to get information from the diffractograms in as-deposited films, we carried out the mathematical subtraction of the halo in the diffractogram and made a Voigt fitting of (222) peak. From the position of the (222) peak, and the Gaussian (w_G) and Lorentzian (w_L) widths obtained from Voigt fitting peak, it is possible to calculate the crystallite size D_{Sch} and the microstrain distribution ε_μ using the expressions [34]: $D_{Sch}=(0.9\lambda)/(w_L\cos\theta)$ and $\varepsilon_\mu=(w_G)/(4\tan\theta')$, respectively. We only estimated the crystallite sizes in as-deposited films with substrate inclinations of 0° and 40° because the low intensity of the peaks in the substrate inclinations of 60° and 80° introduces high inaccuracy. They are $D_{Sch,0°}\approx$ 88 nm, $\varepsilon_{\mu,0°}\approx$0.003 for α=0° and $D_{Sch,40°}\approx$55 nm and $\varepsilon_{\mu,40°}\approx$0.002 for α=40°.

Given the presence of several diffraction peaks in the annealed films, it is possible to calculate the crystallite size D_{WH} and effective maximum strain ε_{WH} by the Williamson–Hall method [35,36] using the expression:

$$\frac{\text{FWHM}}{\lambda}\cos\theta = D_{WH}^{-1} + \frac{\varepsilon_{WH}}{\lambda}\sin\theta \quad (3)$$

where θ and FWHM are the Bragg angle and full width at half maximum, respectively, and λ(=0.15405 nm) is the X-ray wavelength. θ and FWHM are obtained from the fitting of each peak.

The lattice parameter is calculated from the (222) peak using the expression [37]:

$$\alpha_{hkl} = \frac{\lambda\sqrt{h^2+k^2+l^2}}{2\sin\theta} \quad (4)$$

The (222) peak angle does not present a clear tendency. Its average value is $2\theta_{(222)}$=(30.605±0.005)°. The lattice parameter calculated from Eq. (4) for the peak (222) does not show a tendency and its average value is $a_{(222)}$=(1.011±0.001) nm, which is similar to In_2O_3 lattice parameter in the pattern (a_0=1.011 nm) [33], which suggests that the average lattice distortion is not significant. Table 2 gives the results of morphological and structural analysis of annealed samples. The crystallite sizes in as-deposited and annealed films for α=0° and α=40° approximately agree with each other, which is certainly expected, since the annealing temperature and time must not induce significant morphological changes. The crystallite sizes, determined from the Scherrer expression using the Lorentzian width w_L in the (222) peak, agree with those observed from SEM images for the highest substrate inclinations. For α values of 0° and 40°, the crystallite sizes are larger than those calculated from Williamson−Hall expression. However, given that the sizes obtained from Scherrer expression are related to perpendicular direction to the (222) plane, it is possible to infer that the difference is due to preferential growth in that plane direction.

The effective maximum strain ε in annealed films decreases at substrate inclination α=0°, 40° and 60°. However, it increases for α=80°, which is attributed to the increase of the fissures in the film and a subsequent

Table 2 Parameters of ITO thin films from XRD measurements of annealed samples

α/(°)	β_{fit}/(°)	D_{WH}/nm	$\varepsilon_{WH}/10^{-3}$	$2\theta_{(222)}$/(°)	$w_{L(222)}$/(°)	$w_{G(222)}$/(°)	$D_{Sch(222)}$/nm	$\varepsilon_{\mu(222)}/10^{-3}$
0	0	103	4.4	30.607	0.058	0.140	142	2.23
40	20.6	51	3.2	30.598	0.070	0.139	117	2.22
60	25.7	50	3.1	30.608	0.146	0.136	56	2.17
80	29.0	55	3.7	30.597	0.141	0.132	58	2.11

increasing of the surface defects. The microstrain distribution was calculated from the expression for ε_μ in the most intense (222) peak. The microstrain distribution on the (222) plane decreases as the nanocolumn tilt increases, as displayed in Fig. 5. The substantial diminishing of the microstrain distribution with nanocolumn tilt angle increasing means that the effects of the defects and lattice distortions tend to be spatially more located and the neighbor lattice is less affected. That diminution of the microstrain distribution with the nanocolumn tilt angle increasing can be related to the columnar growth taking place in a more organized way, for example, as stacked grains, which results in the reduction of grain boundary in growth direction [8].

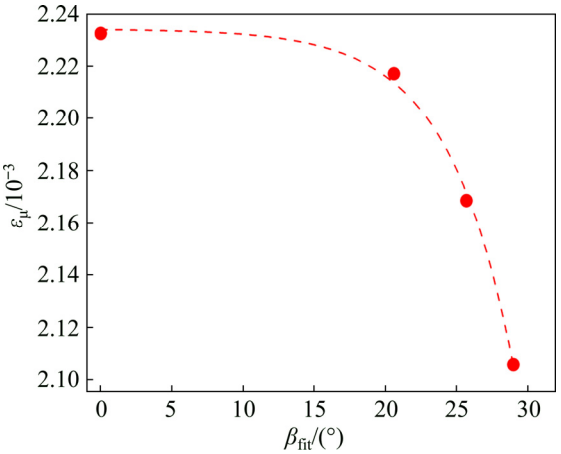

Fig. 5 Microstrain distribution as function of nanocolumn tilt angle

The (222) to (400) peak intensity ratio $I_{(222)}/I_{(400)}$ as a function of the nanocolumn tilt angle is shown in Fig. 6. For β=0°, $I_{(222)}/I_{(400)}$ is similar to that of the In_2O_3 pattern, which suggests random orientation of the crystalline domains like in powder. However, as the nanocolumn tilt angle increases, there is a tendency to grow preferentially in the (222) direction.

3.3 Electrical analysis

From the electrical measurements, it is observed that the major carriers are electrons as expected for ITO films. Table 3 gives the values of resistivity ρ, bulk carrier concentration n_e and the mobility μ. Figure 7 shows the behaviors of resistivity, electron concentration and electron mobility as functions of the nanocolumn tilt

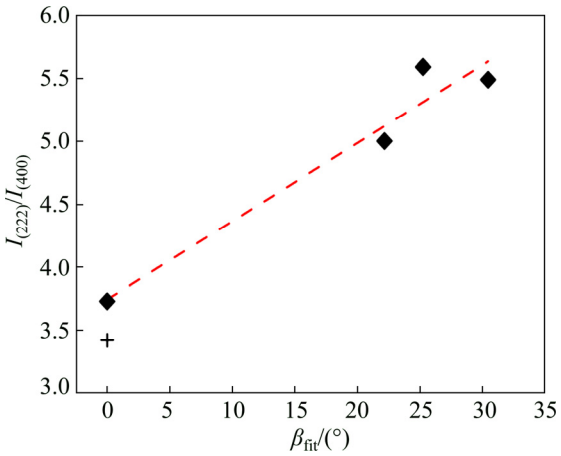

Fig. 6 $I_{(222)}/I_{(400)}$ as function of nanocolumn tilt angle (+ indicates ratio for same peaks in In_2O_3 pattern [33])

Table 3 Electrical measurements in ITO as-deposited and annealed films

Film	β_{fit}/(°)	ρ/(Ω·cm)	n_e/cm^{-3}	μ/(cm^2·V^{-1}·s^{-1})
As-deposited	0	1.62×10^{-3}	1.81×10^{20}	21.4
	20.6	1.13×10^{-3}	2.86×10^{20}	10.01
	25.7	8.96×10^{-2}	2.03×10^{19}	3.43
	29.0	4.49×10^{-2}	4.02×10^{20}	0.346
Annealed	0	3.79×10^{-3}	6.45×10^{20}	2.55
	20.6	4.13×10^{-3}	1.23×10^{21}	1.23
	25.7	7.85×10^{-3}	1.00×10^{21}	0.794
	29.0	1.27×10^{-2}	1.98×10^{20}	2.49

for as-deposited and annealed ITO films. However, in these electrical characterizations, it is found that for high nanocolumn tilt angles the results are inaccurate due to the presence of fissures in the films, which introduce distortions in the measurements. In spite of the uncertainty of their values for high column angle inclination, it is possible to appreciate a general tendency to increase the resistivity and to decrease the electron concentration as the nanocolumn tilt increases. For low nanocolumn tilt angles, the resistivity is higher for annealed films than for as-deposited ones, which can be explained from the fact that the lattice is organized better and the annealing-passivated defects are related to the resistivity. For high tilt angles, the resistivity increases and becomes higher for as-deposited films than for annealed ones.

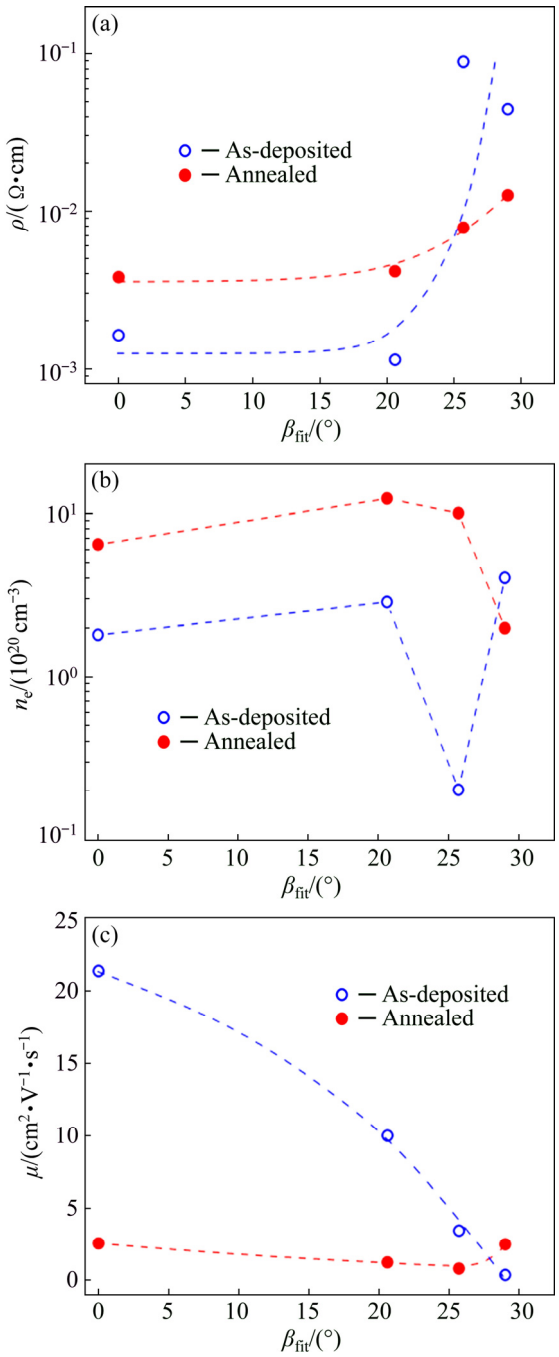

Fig. 7 Behaviors of resistivity (a), carrier concentration (b) and mobility (c) of as-deposited and annealed films

Since no morphological changes are perceived in annealed films respect to as-deposited films for the same nanocolumn tilt angle, it is possible to consider that the main contributions to the variation of electric properties are structural distortions, the punctual defects and the presence of fissures. In a first instance, the increase of resistivity as nanocolumn tilt angle increases is due to the increase of the amount of fissures. In as-deposited films for high nanocolumn tilt angles, high concentrations of surface defects are associated to the fissures. The punctual defects, both on the surface of the fissures and inside the nanocolumns, favor the increase in the concentration of electrons and the conductivity. On the other hand, the proper fissures that can constitute barriers, and the ionizable traps, cause a contrary effect. Therefore, the results depend on the combination of those effects. The diminution of the electron concentration can be associated to the same causes. Simultaneously, the growth of tilted nanocolumns induces the film growth taking place in a more organized way, which can be observed from the diminishing of the strain. The combination of all those features reduces the electron concentration and increases the resistivity, as shown in Figs. 7(a, b).

3.4 Optical analysis

Figure 8 shows the transmittance spectra of the samples obtained at different inclination angles α for as-deposited and annealed films. The average transmission value in the range of 500−1050 nm is T≈80%, and oscilling is between 70% and 90%. The optical band-gap energy, E_g, was calculated employing the Tauc plot and the relation $(\alpha_{abs}h\nu)^2 \propto (h\nu - E_g)$ [38], as displayed in the insets of Fig. 9, where only direct transitions were considered. The band gap energy values increase from 3.587 to 3.961 eV for the as-deposited samples and from 3.748 to 3.927 eV for the annealed samples, as shown in Fig. 9(a). It is noticeable that for non-inclined substrates there is a relatively large difference between the band gap energy of as-deposited film and that of annealed film, ΔE_g≈0.16 eV. However, this difference reduces to nearly zero for high nanocolumnar tilt angles. On the other hand, the band tail parameters calculated by exponential fitting of the region below the band edge [39] are displayed in Fig. 9(b) and suggest that the structural disorder diminishes as the nanocolumn tilt angle increases. However, a coincidence of the tail parameters for as-deposited and annealed films can be perceived as the nanocolumn tilt angle increases. This behavior agrees with that of the microstrain distribution ε_μ. Taking into account the behavior of the electron concentration, we consider that the changes of the band gap energy are not linked to the Moss–Burstein effect.

The band gap energy E_g has been described to be dependent on maximum strain ε by a linear function $E_g(\varepsilon)=E_{g0}+\alpha_d\varepsilon$, where the E_{g0} is the non-strained band gap energy and α_d(=−4.21 eV) is the ITO potential of deformation [40]. However, the band gap energy depends monotonously on the microstrain distribution ε_μ, as shown in Fig. 10(a). Therefore, we can consider that the band gap energy also depends on the microstrain distribution and coarsely it could be described by the expression $E_g(\varepsilon,\varepsilon_\mu)=E_{g0}+\alpha_d(\varepsilon \pm f(\varepsilon_\mu))$ where $f(\varepsilon_\mu)$ is a

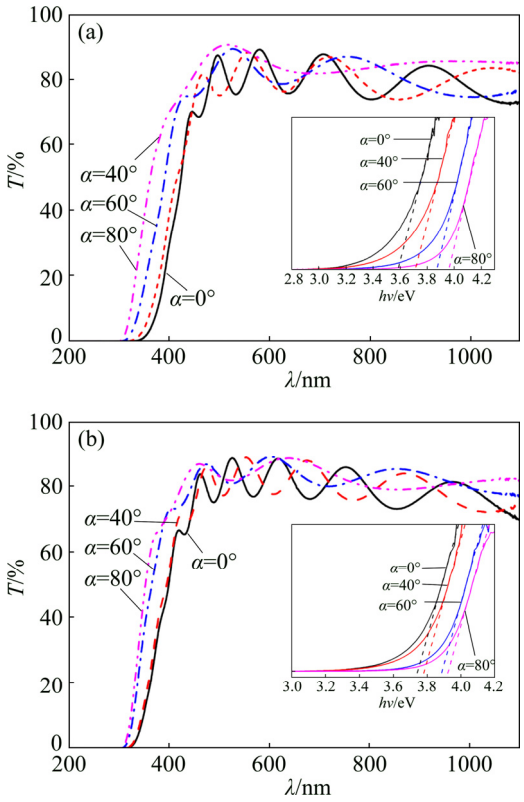

Fig. 8 Transmission spectra of as-deposited (a) and annealed (b) ITO thin films grown at α=0°, 40°, 60° and 80° (Insets show Tauc plots used for determining band gap energies)

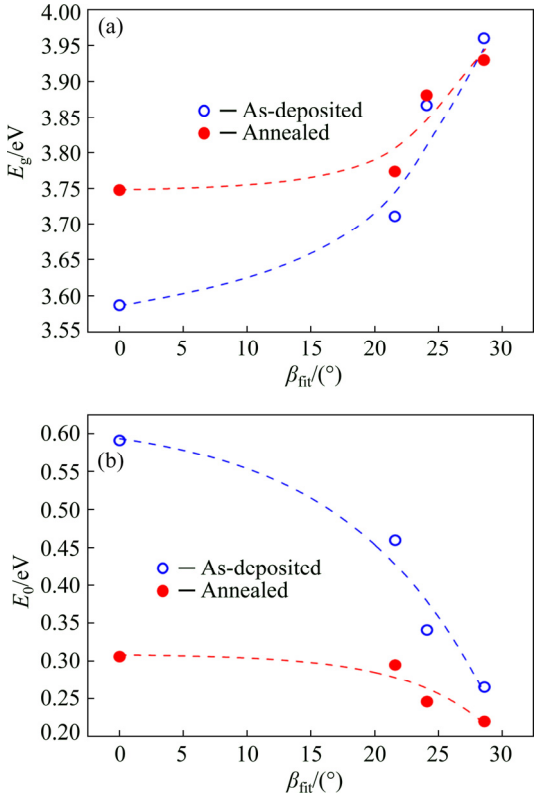

Fig. 9 Band gap energy (a) and band tail parameter (b) of as-deposited and annealed ITO thin films as function of nanocolumn tilt angle

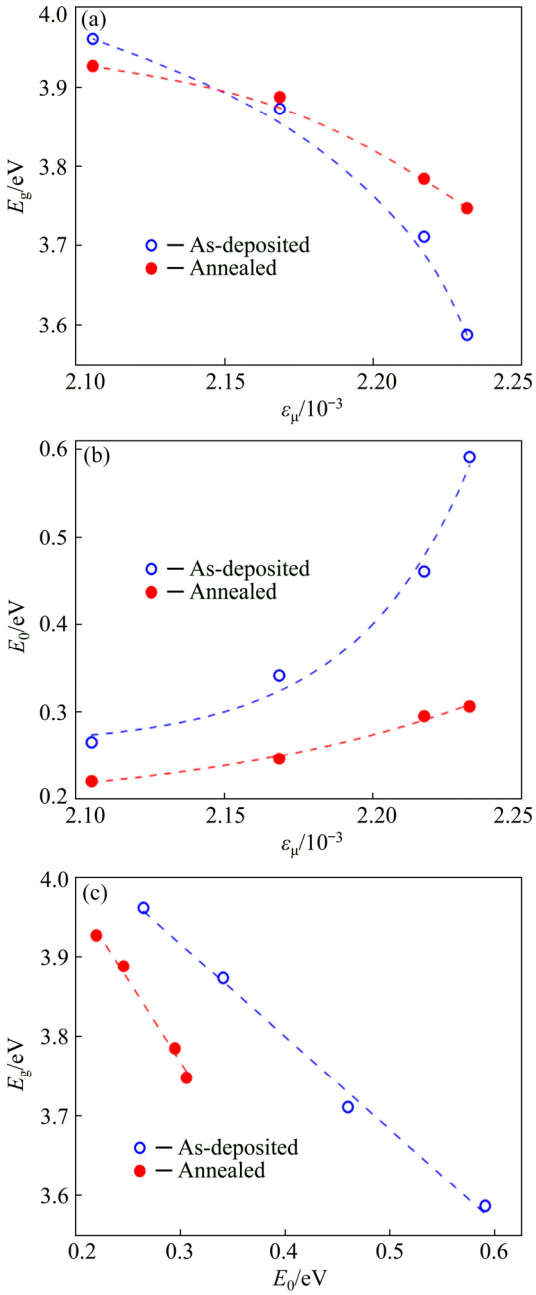

Fig. 10 Band gap energy (a) and band tail parameter (b) of as-deposited and annealed ITO thin films as function of microstrain distribution and correlation between band gap energy and tail parameter (c)

function of the microstrain distribution. However, the absorption profile, from which the band gap energy is determined, would begin from the minimum band gap energy, i.e., $E_{g,min}(\varepsilon,\varepsilon_\mu)=E_{g0}+\alpha_d\varepsilon-\alpha_d f(\varepsilon_\mu)$, and the absorption edge corresponding to higher band gap energies in the range of $\pm\varepsilon_\mu$ would be underlying. Therefore, given that the effective strain is erratic, not linear, and does not show a clear tendency, the behaviour of the band gap energy could be ruled by the behaviour of the microstrain distribution that decreases as the nanocolumn tilt angle increases. It is noticeable that

between α=0° and α=80° the variation of the band gap energy is about 5%, which approximately agrees with variation of the microstrain distribution in the same range of α. The tail parameter E_0, which is related to the material disorder, increases as a function of the microstrain distribution ε_μ, as shown in Fig. 10(b). In this case, we associate the increase of the tail parameter to the increase of surface defects due to the increase of fissures in the films. The apparent contradiction can be explained from the fissures contributing to lattice relaxation. The practically linear E_g dependence on the tail parameter E_0 for as-deposited and annealed films observed in Fig. 10(c) indicates that E_g and E_0 are strongly dependent on the microstrain distribution.

The refractive index (n) is calculated from the equation:

$$n=\frac{1+R}{1-R}+\sqrt{\frac{4R}{(1-R)^2}-k^2} \tag{5}$$

where R is the normal-incident light reflection, k is the extinction coefficient defined as $k=\alpha_{abs}\lambda/4\pi$, α_{abs} is the absorption coefficient and λ is the wavelength. In the region below the band gap energy, the absorption can be disregarded, i.e., $A\rightarrow 0$. Then, the expression $T+R+A=1$ can be reduced to $R=1-T$, from which it is possible to estimate the reflected light [24]. However, generally in those thin films it is not possible to appreciate a defined value of refractive index because of the optical interference. Thus, in order to reduce the effect of these oscillations, we apply the proposed adjustment in Ref. [27] for the determination of the refractive index beginning from the band-tail fitting. Figure 11 exhibits the refractive indexes as a function of the wavelength for different substrate holder tilts in as-deposited and annealed ITO films in the region near the band edge and the low-absorption one. Although the analysis can be extended to the absorption edge energy region, the obtained refractive indexes are not reliable, since the absorption is high, i.e., $A\neq 0$. In this energy region, only approximately estimated values are used.

Figure 12 shows the effective refractive index, n, at λ=800 nm for as-deposited and annealed ITO films. The refractive indexes of as-deposited films are smaller than those of annealed films, and diminish as nanocolumn tilt angle increases. Since there are not morphological changes in the annealed films respect to as-deposited ones for the same nanocolumn tilt angle, it is possible to consider that the main contributions to the variation of the refractive index are structural distortions, the punctual defects and the presence of fissures which produce light scattering [27]. The films, after annealing, present better structural organization and the defects tend to passivate, as discussed before. The combination of both phenomena reduces the light scattering [27],

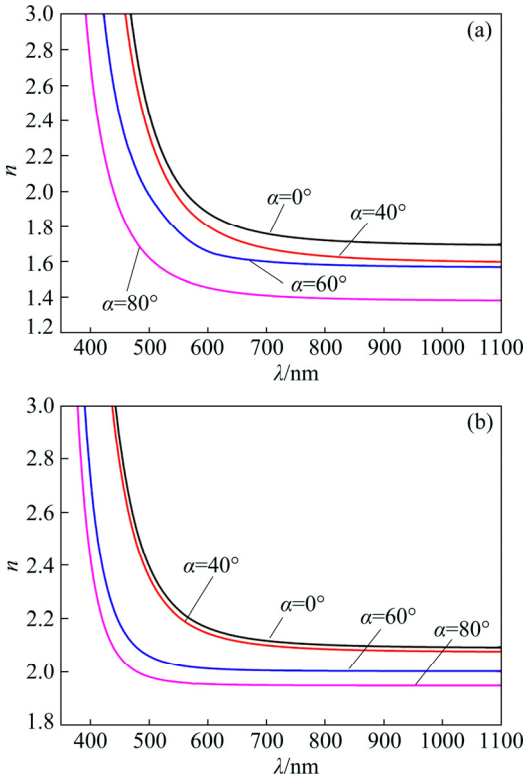

Fig. 11 Refractive index as function of wavelength for different substrate holder tilts in as-deposited (a) and annealed (b) ITO films

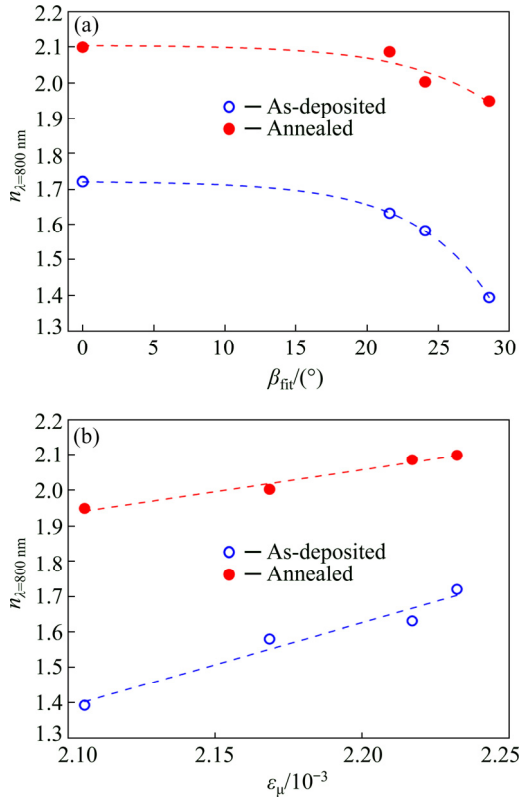

Fig. 12 Refractive indexes at λ=800 nm for as-deposited and annealed ITO films as function of nanocolumn tilt angle (a) and microstrain distribution (b)

although the fissures remain, and the refractive indexes are higher. It is remarkable that the refractive indexes, $n_{as\text{-}dep}$ and n_{anneal}, are linearly dependent on microstrain distribution for as-deposited and annealed films, respectively. Such dependences are described by the following expressions although these expressions are only valid for a minimum value of the microstrain distribution:

$$n_{as-dep}=2360\varepsilon_{\mu}-3.6 \quad (6a)$$

$$n_{anneal}=1240\varepsilon_{\mu}-0.7 \quad (6b)$$

3.5 Porosity analysis

The porosity, P, can be determined from the refractive index in porous, n_p, and non porous, n, materials acording to the expression [41]:

$$P=1-\left(\frac{n_p^2-1}{n^2-1}\right) \quad (7)$$

Porosity from Eq. (7) is P=0 in dense non-porous materials, since $n_p \rightarrow n$. In porous materials, where $n_p \rightarrow 1$, porosity tends to be a maximum value, i.e., $P \rightarrow 1$. Taking into account that the films grown without substrate inclination, i.e., $\alpha=\beta=0°$, are dense, we considered the corresponding refraction index n in as-deposited and annealed films as reference in order to calculate the film porosity. We took the porosity at λ=800 nm, a wavelength where the absorption is so low that can be disregarded. Figure 13 displays the porosity calculated at λ=800 nm as a function of the nanocolumn tilt angle in as-deposited and annealed films. The porosity is related to the shadowing effect and it depends on the substrate inclination angle. Porosity in as-deposited films is found higher than that of annealing films. However, no significant changes of the microstructure, as fissures, can be appreciated in a comparison of as-deposited and annealed films with the same substrate inclination. Thus, we consider that the different refractive indexes for the same substrate inclination are mainly associated to the influence of defects and structural disorder. Besides, the porosity increases as the nanocolumn tilt angle increases due to the increase of the fissures in the films, which, besides, introduce additional scattering effects. Hence, the refractive index diminishes and the porosity increases. Figure 14 shows that the microstrain distribution diminishes as porosity increases. This seeming contradiction can be explained from the fact that the porosity is mainly related to the fissures in the films which increase as the substrate inclinates, and the distribution microstrain depends on defects and lattice distortions which diminish as substrate inclinates. However, this behavior suggests that the fissure formation induces the relaxation of the lattice distortions.

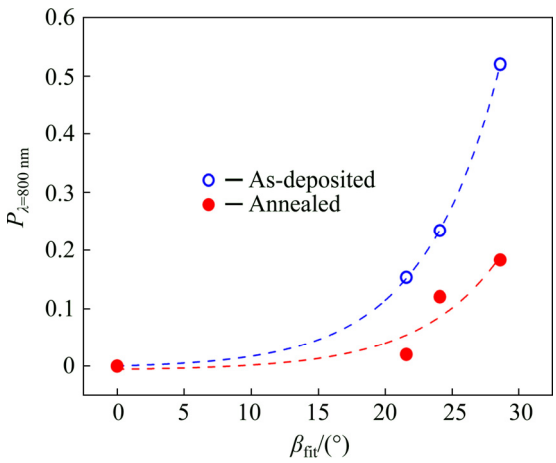

Fig. 13 Porosity calculated at λ=800 nm as function of nanocolumn tilt angle in as-deposited and annealed films

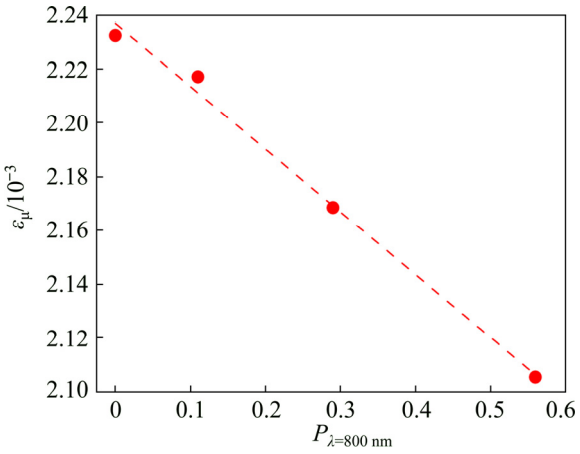

Fig. 14 Correlation between porosity and microstrain distribution in annealed films

The engineering of optical properties in ITO films from morphological modifications can benefit photovoltaic devices by reducing the antireflecting effect between the TCO and the electron transfer layers, although it can be used in other optoelectronic devices. Under morphological modifications and convenient annealing, it is possible to tune the effective ITO refractive index in an approximate range of 1.4−2.1, which includes the refractive index of glasses, and the band gap energy can change from 3.6 to almost 4 eV. It is noticeable, and as a subsequent deduction from the dependences of electrical and optical properties, that rather than the effective or maximum microstrain, the predominant influence comes from the microstrain distribution given by the spatial dispersion of the lattice distortions due to structural disorder and defects. A dependence of optical properties on the microstrain distribution was also found in CdTe films grown by close space sublimation (CSS) with OAD [8], which induces to think it is a generalized physical feature.

4 Conclusions

(1) By using the OAD technique combined with thermal annealing, the optical properties can be tuned according to the substrate inclination and, consequently, to the tilted column morphology.

(2) Fissures that confer porosity to the films grown with high substrate inclination are observed and play an important role in the optical property tuning.

(3) In as-deposited films, the refractive index could be changed between 1.7 in films grown with non-inclined substrate, i.e., 0° tilted columns and 1.4 in films with 29° tilted columns. In ITO films annealed at 250 °C, the refractive index changes from 2.1 to 1.95 in films with the same range of column tilt angles.

(4) The band gap energy increases up to almost 0.4 eV as a function of the nanocolumn tilt angle.

(5) These results allow the tuning of optical properties, mainly the refractive index, by morphology engineering in order to enhance the antireflecting effect in ITO films, although other application can be found in photonics and optoelectronics.

Acknowledgments

The authors acknowledge Oswaldo Gomez, Mario Herrera, Dora Huerta and Daniel Aguilar for technical support and Lourdes Pinelo for secretarial assistance. This work has been supported by the Project No. CB/2012/178748 CONACYT/México.

References

[1] O'DWYER C, SOTOMAYOR TORRES C M. Epitaxial growth of an antireflective, conductive, graded index ITO nanowire layer, frontiers in physics [J]. Interdiscipl Phys, 2013, 1: 18.

[2] JO Y J, HONG C H, KWAK J S. Improved electrical and optical properties of ITO thin films by using electron beam irradiation and their application to UV-LED as highly transparent p-type electrodes [J]. Curr Appl Phys, 2011, 11: s143−s146.

[3] PARSIANPOUR E, RAOUFI D, ROOSTAEI M, SOHRABI B, SAMAVAT F. Characterization and structural property of indium tin oxide thin films [J]. Adv Mater Phys Chem, 2017, 7: 42−57.

[4] HONGSINGTHONG A, YUNAZ I A, MIYAJIMA S, KONAGAI M. Preparation of ZnO thin films using MOCVD technique with D_2O/H_2O gas mixture for use as TCO in silicon-based thin film solar cells [J]. Sol Energ Mat Sol C, 2011, 95: 171−174.

[5] AHN M H, CHO E S, KWON S J. Characteristics of ITO-resistive touch film deposited on a PET substrate by in-line DC magnetron sputtering [J]. Vacuum, 2014, 101: 221−227.

[6] VAISHNAV V S, PATEL S G, PANCHAL J N. Development of ITO thin film sensor for detection of benzene [J]. Sensor Actuat B−Chem, 2015, 206: 381−388.

[7] RASHED A R, GUDULLUOGLU B, YUN H W, HABIB M, BOYACI I H, HONG S H, OZBAY E, CAGLAYAN H. Highly-sensitive refractive index sensing by near-infrared metatronic nanocircuits [J]. Sci Rep−UK, 2018, 8: 11457.

[8] DAZA L G, CANCHÉ-CABALLERO V, CHAN Y DÍAZ E, CASTRO-RODRÍGUEZ R, IRIBARREN A. Tuning optical properties of CdTe films with nanocolumnar morphology grown using OAD for improving light absorption in thin-film solar cells [J]. Superlattice Microst, 2017, 111: 1126−1136.

[9] MANZOOR S, ZHENGSHAN J Y, ALI A, ALI W, BUSH K A, PALMSTROM A F, HOLMAN Z C. Improved light management in planar silicon and perovskite solar cells using PDMS scattering layer [J]. Sol Energ Mat Sol C, 2017, 173: 59−65.

[10] LAU J Z, WONG B T. Indium tin oxide-based selective emitter for nano-gap thermophotovoltaic applications [J]. Int J Nano Res−Sw, 2017, 49: 127−148.

[11] SALEHI A, HO S, CHEN Y, PENG C, YERSIN H, SO F. Highly efficient organic light−emitting diode using a low refractive index electron transport layer [J]. Adv Opt Mater, 2017, 5: 1700197.

[12] SCHUSTER M, GROß S, ROIDER F, MAKSIMENKO I, WELLMANN P J. Tuning electrical and optical properties of transparent conductive thin films using ITO and ZnO nanoparticles, sol−gel−ZnO and Ag nanowires [J]. Int J Nanoparticles Nanotech, 2017, 3: 013.

[13] OH M, JEONG Hyeon-Jun, JEONG Mun-Seok, AHN Kwang-Soon, KIM Kyoung-Kook, RYOU Jae-Hyun, KIM H. Functional hybrid indium-tin-oxide transparent conductive electrodes for light-emitters [J]. J Alloy Compd, 2017, 724: 813−819.

[14] KHAN I, BAUCH M, DIMOPOULOS T, DOSTALEK J. Nanostructured as-deposited indium tin oxide thin films for broadband antireflection and light trapping [J]. Nanotechnology, 2017, 28: 325201.

[15] ALAM M J, CAMERON D C, Optical and electrical properties of transparent conductive ITO thin films deposited by sol–gel process [J]. Thin Solid Films, 2000, 378: 455−459.

[16] BAGHI R, ZHANG K, WANG S, HOPE-WEEKS L J. Conductivity tuning of the ITO sol−gel materials by adjusting the tin oxide concentration, morphology and the crystalline size [J]. Micropor Mesopor Mat, 2017, 244: 258−263.

[17] CHO H, YUN Young-Hoon. Characterization of indium tin oxide (ITO) thin films prepared by a sol−gel spin coating process [J]. Ceram Int, 2011, 37: 615−619.

[18] BABU B M, VADIVEL S. High performance humidity sensing properties of indium tin oxide (ITO) thin films by sol–gel spin coating method [J]. J Mater Sci−Mater El, 2017, 28: 2442−2447.

[19] RAJ E S, CHOY K L. Microstructure and properties of indium tin oxide films produced by electrostatic spray assisted vapour deposition process, a new investigation of oxygen flow influence on ITO thin films by magnetron sputtering [J]. Mater Chem Phys, 2003, 82: 489−492.

[20] CHEN A, ZHU K, ZHONG H, SHAO Q, GE G. A new investigation of oxygen flow influence on ITO thin films by magnetron sputtering [J]. Sol Energ Mat Sol C, 2014, 120: 157−162.

[21] HEO Kyong-Chan, SOHN Y, GWAG Jin-Seog. Effects of an additional magnetic field in ITO thin film deposition by magnetron sputtering [J]. Ceram Int, 2015, 41: 617−621.

[22] LEBBAD A, KERKACHE L, LAYADI A, LEROY F, ALSHEHRI B, DOGHECHE E. Surface morphology, structural and electrical properties of RF-sputtered ITO thin films on Si substrates [J]. Bull Mater Sci, 2015, 41: 74.

[23] LI Q, ZHANG Y, FENG L, WANG Z, WANG T, YUN F. Investigation of the influence of growth parameters on self-catalyzed ITO nanowires by high RF-power sputtering [J]. Nanotechnology, 2018, 29: 165708.

[24] KIM Hoon-Young, CHOI Won-Suk, JI Suk-Young, SHIN Young-Gwan, JEON Jin-Woo, AHN S, CHO Sung-Hak. Morphologies of femtosecond laser ablation of ITO thin films using gaussian or quasi-flat top beams for OLED repair [J]. Appl Phys A, 2018, 124: 123.

[25] CUI Hai-ning, TEIXEIRA V, MENG Li-jian, MARTINS R, FORTUNATO E. Influence of oxygen/argon pressure ratio on the morphology, optical and electrical properties of ITO thin films deposited at room temperature [J]. Vacuum, 2008, 82: 1507−1511.
[26] SIVAKUMAR R, KUMAR M, SANJEEVIRAJA C, SOM T. Tuning electro-optical properties of pulsed dc magnetron sputtered indium tin oxide thin films: Effects of pulsing frequency and annealing [J]. J Mater Sci−Mater El, 2017, 28: 1409−1418.
[27] MARTÍN-TOVAR E A, DENIS-ALCOCER E, CHAN Y, DÍAZ E, CASTRO-RODRÍGUEZ R, IRIBARREN A. Tuning of refractive index in Al-doped ZnO films by rf-sputtering using oblique angle deposition [J]. J Phys D: Appl Phys, 2016, 49: 295302.
[28] BARRANCO A, BORRAS A, GONZALEZ-ELIPE A R, PALMERO A. Perspectives on oblique angle deposition of thin films: From fundamentals to devices [J]. Prog Mater Sci, 2016, 76: 59−153.
[29] YÜZÜAK G D, COŞKUN Ö D. The effect of annealing on the structural, electrical, optical and electrochromic properties of indium-tin-oxide films deposited by RF magnetron sputtering technique [J]. Optik, 2017, 142: 320−326.
[30] TERZINI E, THILAKAN P, MINARINI C. Properties of ITO thin films deposited by RF magnetron sputtering at elevated substrate temperature [J]. Mat Sci Eng B−Adv, 2000, 77: 110–114.
[31] CRUZ L R, LEGNANI C, MATOSO I G, FERREIRA C L, MOUTINHO H R. Influence of pressure and annealing on the microstructural and electro-optical properties of RF magnetron sputtered ITO thin films [J]. Mater Res Bull, 2004, 39: 993−1003.
[32] HU Y, DIAO X, WANG C, HAO W, WANG T. Effects of heat treatment on properties of ITO films prepared by rf magnetron sputtering [J]. Vacuum, 2002, 75: 183−188.
[33] JCPDS-International Centre for Diffraction Data 2003 PCPDFWIN v. 2.4 Chart No. 71-2194 [S]. 2003.
[34] MITTEMEIJER E J, WELZEL U. Modern diffraction methods [M]. Weinheim, Germany: Wiley-VCH Verlag & Co, 2013.
[35] WILLIAMSON G K, HALL W H. X-ray line broadening from filed aluminium and wolfram [J]. Acta Metall, 1953, 1: 22−31.
[36] MOTE V D, PURUSHOTHAM Y, DOLE B N. Williamson−Hall analysis in estimation of lattice microstrain in nanometer-sized ZnO particles [J]. J Theor Appl Phys, 2012, 6: 6.
[37] CULLITY B D. Elements of X-ray diffraction [M]. Massachusetts, USA: Addison-Wesley Publishing Company, Inc, 1956.
[38] TAUC J, GRIGOROVICI R, VANCU A. Optical properties and electronic structure of amorphous germanium [J]. Phys Status Solidi B, 1966, 15: 627−637.
[39] IRIBARREN A, CASTRO-RODRÍGUEZ R, SOSA V, PEÑA J L. Modeling of the disorder contribution to the band-tail parameter in semiconductor materials [J]. Phys Rev B, 1999, 60: 4758−4762.
[40] ZHANG K H L, LAZAROV V K, VEAL T D, OROPEZA F E, MCCONVILLE C F, EGDELL R G, WALSH A. Thickness dependence of the strain, band gap and transport properties of epitaxial In_2O_3 thin films grown on Y-stabilised ZrO_2(111) [J]. J Phys: Condens Matter, 2011, 23: 334211.
[41] YOLDAS B E. Investigations of porous oxides as an antireflective coating for glass surfaces [J]. Appl Optics, 1980, 19: 1425−1429.

斜角沉积和热处理对射频溅射 ITO 薄膜光学性能的影响

L. G. DAZA[1], M. ACOSTA[2], R. CASTRO-RODRÍGUEZ[1], A. IRIBARREN[3]

1. Department of Applied Physics, CINVESTAV-IPN, Unity Mérida. 97310 Mérida, Yucatán, México;
2. Materials Science Laboratory, Faculty of Engineering, University of Yucatan, CP 97130 Mérida, Yuc., México;
3. Instituto de Ciencia y Tecnología de Materiales, Universidad de La Habana, Zapata s/n esq. G, Vedado, Plaza, La Habana 10400, Cuba

摘　要：运用射频溅射斜角沉积(OAD)制备铟锡氧化物(ITO)薄膜，对薄膜在 250 °C 下进行热处理，采用基体倾斜和退火相结合的方法对材料的形貌和结构进行改性，从而改变材料的光学性能。对薄膜的形貌表征观察到倾斜的纳米柱、柱间裂纹和结构变化。沉积的薄膜具有非晶成分，结构无序；退火后薄膜被晶化，更加有序；薄膜 XRD 衍射图样与 In_2O_3 的立方结构相对应。随着纳米柱倾角的变化，沉积薄膜的折射率可以提高到 0.3，退火薄膜的折射率可以提高到 0.15。同样，由于微应变的减少，带隙能增加到 0.4 eV 左右。结果还发现，微应变分布与晶格畸变、缺陷和薄膜中裂纹的存在有关，因此，可以通过改变薄膜的形貌实现对其光学性质的调整。

关键词：斜角沉积；ITO 薄膜；纳米柱形态；微应变分布；光学性质

(Edited by Bing YANG)